CrossMark
click for updates

Rational tuning of the cation ratio in metal oxide semiconductor nanofibers for low-power neuromorphic transistors

Haofei Cong[1†], Yu Chang[1†], Ruifu Zhou[2], Wenxin Zhang[1], Guangxin Sun[1], Peilong Xu[1], Yuanbin Qin[3], Seeram Ramakrishna[4], Xuhai Liu[2*] and Fengyun Wang[1*]

ABSTRACT   Wide-bandgap metal oxide semiconductor (MOS) nanofiber neuromorphic transistors (NFNTs) can be potentially used to construct low-power bio-inspired artificial circuits. However, the cation ratio of MOS used for NFNTs is mostly adopted without detailed reasons in literature. In this study, we have for the first time focused on systematically tuning the cation ratio of indium zinc oxide (InZnO)-based NFNTs, fabricated by a low-cost electrospinning technique combined with a facile nanofiber transfer process. These electrical-driven NFNTs based on double-cation InZnO nanofibers can greatly simplify experimental procedures. Among the cation ratios of $In_xZn_{1-x}O$ (x = 0.6, 0.7, 0.8, 0.9), we found that NFNTs based on $In_{0.7}Zn_{0.3}O$ exhibited the lowest excitatory postsynaptic currents and offered electrical benefits for low-power operations and synaptic function simulations. The rational tuning of MOS nanofiber composition opens the door for high-performance low-power NFNTs.

Keywords: power consumption, artificial synapse, artificial neuron, phase transition, excitatory postsynaptic current

INTRODUCTION

Artificial general intelligence covers many interdisciplinary subjects with an emphasis on developing new building blocks of in-memory computing hardware [1]. In this regard, the progress of producing bio-inspired neuromorphic transistors has been greatly accelerated in the past decade [2,3], due to the plausible features of synchronous receiving and reading stimuli [4], superior synaptic weight controllability [5], co-integration of artificial synapses and neurons [6], etc. Among the urgent aspects of improving neuromorphic transistors, the effective decrease of transistor power consumption is of vital importance. Multiple methods have been proposed to mitigate the power consumption of neuromorphic transistors, such as integrating composite electrolytes to enhance ionic conductivity and the capacitance of electric double layer (EDL) [7], constructing three-dimensional (3D) electrolyte/semiconductor interfaces for improved contact surface [8], rigorously selecting the combination of active material and versatile structure design [9], and directly tuning the active semiconducting materials [10–13].

Among them, configuring the active semiconducting material is a universal method to lower the device power consumption, which can also serve as the basis for further improvement if coupled with other aforementioned methods.

Particularly, the composition of wide-bandgap metal oxide semiconductors (MOSs) can be easily tuned to exhibit beneficial features, such as low cost, high environmental stability together with versatile superior optoelectronic characteristics, which have been implemented in diverse applications, including gas sensors [14,15], photoconductors [16,17], transistor-based electronics [18,19], and neuromorphic transistors [20–22]. Especially regarding neuromorphic transistors, a wide range of studies have reported low-power neuromorphic transistors based on MOS thin films [23–25], in which the cation ratio was adopted without detailed reasons. Also importantly, unlike the MOS thin films, MOSs with 1D nanofiber configurations can be endowed with larger surface-to-volume ratios together with more superior charge transport characteristics [26,27]. Within the aspect of device capability for various processing and integrating requirements, 1D nanofibers can greatly facilitate the fabrication of flexible and stretchable devices for new-generation wearable electronics [28,29]. In addition, given the resemblance of the biological axon and the artificial nanofiber, more sophisticated bio-inspired neural networks could be constructed based on nanofiber neuromorphic transistors (NFNTs) [30]. Therefore, gaining a better understanding of how to systematically lower the power consumption of NFNTs will bring us closer to obtaining cutting-edge bio-inspired neural circuits.

Our group has recently fabricated NFNTs based on double-cation indium zinc oxide (InZnO) nanofibers and compared the characteristics obtained from nanofiber arrays (NFAs) with nanofiber networks [31]. However, the rational tuning of the cation ratio should be further evaluated. Zhu *et al.* [32] reported optical-driven neuromorphic transistors based on triple-cation indium gallium zinc oxide (IGZO) nanofibers, in which the short-term plasticity can be adjusted to become long-term plasticity by tuning the indium ratio within the IGZO channel. Looking only at the impact of specific cation ratio tuning on device power consumption, electrical-driven NFNTs based on double-cation MOS nanofibers may be more suitable for elucidating the charge carrier concentration and crystalline phase

[1] College of Physics and State Key Laboratory of Bio Fibers and Eco Textiles, Qingdao University, Qingdao 266071, China
[2] College of Microtechnology & Nanotechnology, Qingdao University, Qingdao 266071, China
[3] School of Materials Science and Engineering, Xi'an Jiaotong University, Xi'an 710000, China
[4] Center for Nanofibers & Nanotechnology Department of Mechanical Engineering, National University of Singapore, Singapore 117574, Singapore
† These authors contributed equally to this work.
* Corresponding authors (emails: xuhai@qdu.edu.cn (Liu X); fywang@qdu.edu.cn (Wang F))

transition resulting from the rational tuning of cation ratio.

In this work, we have focused on systematically tuning the cation ratio of InZnO-based NFNTs, fabricated by a low-cost electrospinning technique combined with a facile nanofiber transfer process. The electrical-driven NFNTs based on double-cation InZnO nanofibers can greatly simplify the experimental procedures, e.g., neglecting more complicated charge carrier dynamics and crystalline phase transition induced by optical stimuli [32]. Among the cation ratios of $In_xZn_{1-x}O$ ($x = 0.6, 0.7, 0.8, 0.9$), we found that NFNTs based on $In_{0.7}Zn_{0.3}O$ exhibited the lowest excitatory postsynaptic currents (EPSCs) and offered electrical benefits for low-power operation and synaptic function simulation. The reasons fall into two broad categories. Firstly, the X-ray photoelectron spectroscopy (XPS) measurements indicate that the content of oxygen vacancies decreases with increased Zn content, leading to reduced free charge carrier concentration and subsequent low EPSC magnitude. Secondly, the X-ray diffraction (XRD) spectra reveal that the rhombohedral hexahedral phase of In_2O_3 with better conductivity gradually dominates with increased Zn content. The balancing point between these two impacts with subsequent excellent neuromorphic characteristics indicates that the rational tuning of the MOS nanofiber composition opens the door for high-performance low-power NFNTs. This study, centering on lowering power consumption of MOS NFNTs, might also provide valuable insight into low-power synaptic transistors based on other materials.

EXPERIMENTAL SECTION

Polyvinylpyrrolidone (PVP, 0.8 g, M_w of 1,300,000 g mol^{-1}) was dissolved in 5 mL of N,N-dimethyl formamide (DMF, 99.9%, Aladdin) to form a homogenous solution, which was followed by the addition of indium chloride tetrahydrate ($InCl_3 \cdot 4H_2O$, 99.9%, Aladdin) and zinc chloride ($ZnCl_2$, 99.99%, Aladdin). The mole ratio of Zn, i.e., mole (Zn)/[mole (Zn) + mole (In)] was tuned from 10% to 40% by adjusting the content of $ZnCl_2$. The mixed solution was then stirred magnetically for 12 h to obtain the precursors, which are denoted as $In_{0.6}Zn_{0.4}O$, $In_{0.7}Zn_{0.3}O$, $In_{0.8}Zn_{0.2}O$ and $In_{0.9}Zn_{0.1}O$, respectively. Lithium perchlorate ($LiClO_4$, Aladdin) was mixed with polyethylene oxide (PEO, Aladdin) in a mass ratio of 8:1. The mixture was then dissolved in 5 mL of acetonitrile (CH_3CN, 99.9%, Aladdin) and stirred for 12 h at room temperature. The capacitance density of the $LiClO_4$/PEO electrolyte reached 6.2 μF cm^{-2} at 20 Hz, as shown in Fig. S1.

The sliced Si/SiO_2 substrates were cleaned in an ultrasonic bath using deionized water, acetone and ethanol for 10 min sequentially, and then blown dry with nitrogen. The InZnO NFAs were electrospun with a direct current (DC) voltage of 16.5 kV at a flow rate of 0.008 mL min^{-1}. Using a large electric field, the InZnO nanofibers can be arranged neatly between two parallel metal sheets to form NFAs [33]. This was followed by the rapid movement of the Si/SiO_2 substrate, which ensured a uniform distribution of the transferred InZnO nanofibers. After spinning for 15 s at room temperature and humidity of 50%, the samples were heated at 150°C for 10 min and treated with ultraviolet (UV) irradiation (1 kW, 290–320 nm) for 40 min, which enhanced the adhesion of the nanofibers to the substrate. To remove PVP and Cl$^-$ from the precursor, the prepared nanofibers were annealed at 500°C for 2 h with a fixed heating rate of 5°C min^{-1}. Finally, Al electrodes with a thickness of

100 nm were deposited by thermal evaporation using a shadow mask (width/length = 1000/100 μm) as the source and drain (S/D). Fig. S2 presents an optical image of the electrode arrays including the nanofibers. Finally, 50 μL of ionic liquid was cast onto the channel region to cover the InZnO NFAs. The fabricating process of the synaptic transistors is schematically demonstrated in Fig. S3.

The chemical compositions and the crystal structures of $In_xZn_{1-x}O$ nanofibers were investigated by XPS (PHI5000 Versaprobe III) and XRD (Rigaku D/max-rB). The scanning electron microscopy (SEM, Nova Nano SEM450, 15 kV), transmission electron microscopy (TEM, JEOL JEM-2100plus, operated at 200 kV) and high-resolution TEM (HRTEM) were used to measure the morphology of the prepared materials. The element distribution was investigated by energy-dispersive X-ray spectroscopy (EDS Oxford Instrument and EDAX Inc). All the electrical characteristics and synaptic functions of the synaptic transistors were tested with a Keithley B2912A I–V parametric analyzer in atmosphere at room temperature. The specific device measurement conditions were as follows: with the S/D in contact with two separate tungsten probes and the gate probe in contact with an ionic liquid electrolyte, the electrical signals were acquired by a Keysight B2912A semiconductor parameter analyzer at room temperature, 45% ambient humidity and in the dark.

RESULTS AND DISCUSSION

Device configuration

Fig. 1a illustrates the simplified biology synapse among the connections of two neurons. Nerve impulses are transmitted from the pre-synaptic neuron to the post-synaptic neuron. In this process, synaptic vesicles release neurotransmitters into the synaptic cleft, which bind to specific receptors on the post-synaptic membrane to open ion channels. The directional movement of ions drives variations in membrane potential to generate a signal [34]. Likewise, in the artificial neuromorphic transistors based on InZnO NFAs, the synaptic signal transmission is imitated by executing decoupled electrical write/read operations. The NFNT consists of a top probe gate, $LiClO_4$/PEO electrolyte dielectric, S/D electrodes and an Si/SiO_2 substrate, as illustrated in the simplified configuration of Fig. 1b. The top gate acts as a pre-synaptic membrane to drive ion transport in the electrolyte, and the InZnO NFAs are the artificial equivalent of the post-synaptic membrane. The output signal is transmitted by the S/D electrodes.

Specifically, as demonstrated in Fig. 1c, when a pulse voltage is applied to the top probe gate, the lithium ions in the electrolyte are pushed towards the electrolyte/InZnO interface and the anions are pushed towards the electrolyte/top gate interface due to the corresponding electric field. Lithium ions can induce electrons in the channel, thereby forming EDL [35]. When a gate voltage pulse (V_{gs}) is applied to the device, most potential of the external electric field falls on the Helmholtz plane [36], leading to a large capacitance of the EDL, with corresponding low operating voltage and subsequent reduced energy consumption. In a biological neural circuit, the EPSCs can be obtained by tuning the cell membrane potential *via* the opening and closing of the ion channels. Correspondingly, in the artificial synapse, when the pulse voltage is removed, the lithium ions gathered in the vicinity of the channel gradually return to the electrolyte due
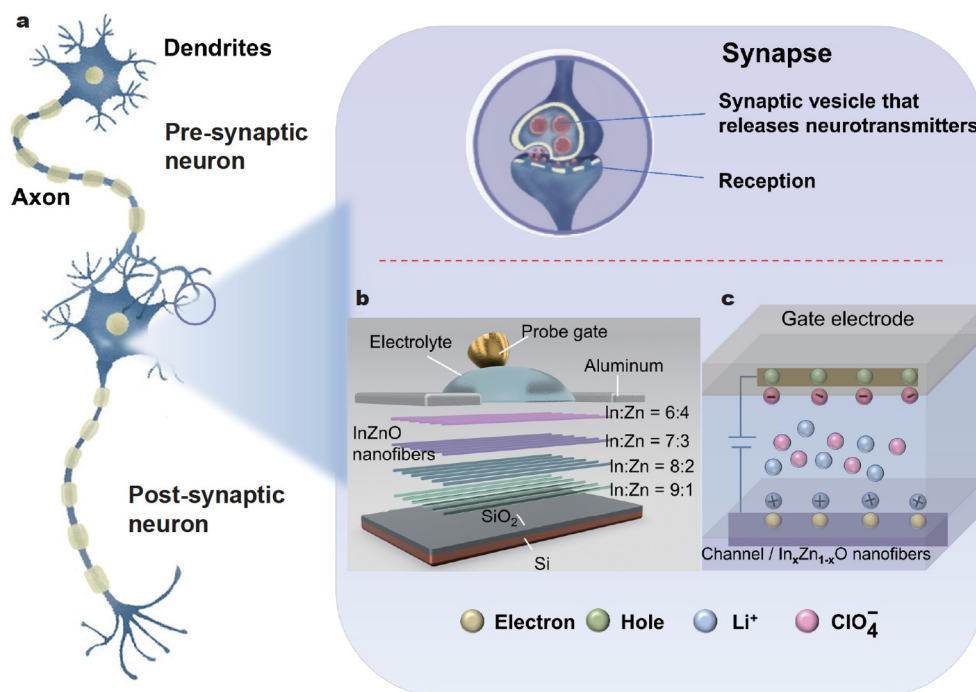
Figure 1 (a) Schematic illustration of signal transmission between two exemplified neurons, with the highlighted synaptic structure. (b) Device configuration of the electrolyte-gated artificial synaptic transistor based on $In_xZn_{1-x}O$ (x = 0.6, 0.7, 0.8, 0.9) nanofibers. (c) EDL triggered by the ion migration process under the regulation of the pulse voltage.

to the concentration gradient. This slow relaxation process leads to a gradual decrease in the concentration of electrons, resulting in a gradual decrease in the current output from the S/D electrodes. This adjustment of channel conductance induced by the ions resembles the biological synaptic signaling process [37].

Selection of low-power $In_xZn_{1-x}O$ (x = 0.6, 0.7, 0.8, 0.9) NFAs

Next, we investigated the underlying mechanism of the best performance of $In_{0.7}Zn_{0.3}O$ NFNTs after rational tuning of the cation ratio. Firstly, an excessive carrier concentration in the In_2O_3 intrinsic semiconductor leads to a high oxygen vacancy (O_{Voc}) concentration [19]. By adding Zn^{2+} to the MOS, the excessive carrier concentration can be suppressed, thereby partly reducing the oxygen vacancies. The $In_{0.8}Zn_{0.2}O$ and $In_{0.9}Zn_{0.1}O$ semiconductors possess high charge carrier concentrations with a corresponding negatively shifted threshold voltage (V_{th}), which is defined as the gate voltage required to create a channel of electrons or holes in the semiconductor material.

Secondly, in terms of crystalline phase transition, when the indium content decreases from $In_{0.9}Zn_{0.1}O$ to $In_{0.6}Zn_{0.4}O$, the rhombohedral phase of In_2O_3 gradually dominates in the cubic phase. Since the rhombohedral phase corresponds to higher conductivity due to its better packing of the anion layers [38], the electrical conductivity of $In_{0.7}Zn_{0.3}O$ is lower than that of $In_{0.6}Zn_{0.4}O$, and the V_{th} of the $In_{0.6}Zn_{0.4}O$ will be negatively shifted with a higher current value.

We then experimentally verified this point using systematic XPS and XRD measurements. Firstly, in order to investigate the O_{Voc} concentration contained in $In_{0.6}Zn_{0.4}O$, $In_{0.7}Zn_{0.3}O$, $In_{0.8}Zn_{0.2}O$ and $In_{0.9}Zn_{0.1}O$, respectively, XPS measurements were taken under the same conditions. Fig. 2a–d show the relative O 1s spectra of $In_xZn_{1-x}O$ NFAs with In:Zn molar ratios

of 6:4, 7:3, 8:2 and 9:1, respectively. The O 1s spectra exhibit $O_{Lat.}$, $O_{Voc.}$ and $O_{Chem.}$ peaks, for which 529.1 ± 0.1 eV corresponds to the lattice oxygen ($O_{Lat.}$), 530.1 ± 0.1 eV corresponds to O_{Voc}, and 531.6 ± 0.1 eV corresponds to the surface chemisorbed oxygen ($O_{Chem.}$). As summarized in Table S1, the O_{Voc} concentrations of $In_{0.6}Zn_{0.4}O$, $In_{0.7}Zn_{0.3}O$, $In_{0.8}Zn_{0.2}O$ and $In_{0.9}Zn_{0.1}O$ are 27.02%, 37.81%, 39.24%, and 40.69%, respectively. Increasing the mass of In and decreasing the mass of Zn causes the number of $O_{Voc.}$ to gradually increase. The number of electrons in n-type semiconductor materials is closely related to $O_{Voc.}$, because the production of $O_{Voc.}$ is accompanied by the production of two free electrons. The formation of oxygen vacancies is mainly due to the detachment of oxygen atoms in metal oxides from the lattice, resulting in the absence of oxygen and the formation of vacancies. Importantly, because the binding energy of Zn–O is larger than that of In–O [19], the Zn–O bond is much more difficult to break. Therefore, more Zn–O bonds correlate with less $O_{Voc.}$, which leads to the fact that the density of $O_{Voc.}$ in $In_{0.7}Zn_{0.3}O$ is less than that of $In_{0.6}Zn_{0.4}O$. The increase of $O_{Voc.}$ provides more electrons for the $In_xZn_{1-x}O$ nanofiber semiconductor channel layer, i.e., the carrier concentration is increased. Under the same biasing condition, the cations move towards the electrolyte/$In_xZn_{1-x}O$ (x = 0.6, 0.7, 0.8, 0.9) interface, inducing electrons in the nanofibers. In this process, the concentration of oxygen vacancies can be reduced by the modulation of the In:Zn molar ratio, thereby reducing the induced electrons.

To further investigate the effect of In:Zn molar ratio modulation on the EPSC magnitude, the crystalline phase and composition of $In_{0.6}Zn_{0.4}O$, $In_{0.7}Zn_{0.3}O$, $In_{0.8}Zn_{0.2}O$ and $In_{0.9}Zn_{0.1}O$ NFAs were examined by XRD patterns. It should be noted that the peaks of cubic-In_2O_3 and rhombohedral-In_2O_3
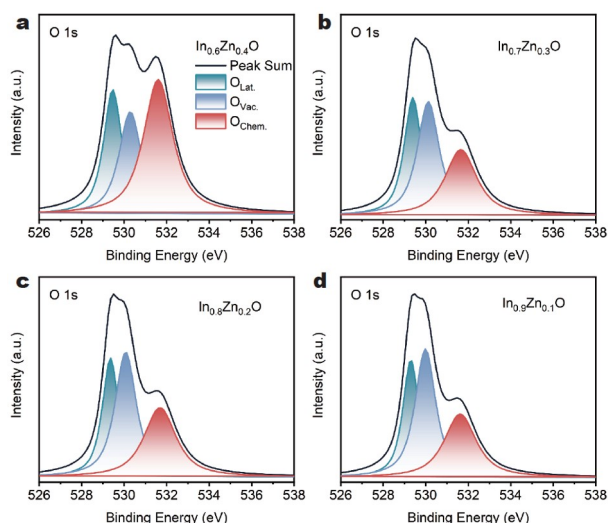
Figure 2 XPS spectra of $In_xZn_{1-x}O$ nanofibers with (a) $x = 0.6$, (b) $x = 0.7$, (c) $x = 0.8$, (d) $x = 0.9$.

were observed using the XRD of the four control samples, as shown in Fig. 3a. With an increasing In:Zn molar ratio, the diffraction peaks of cubic-In_2O_3 gradually weaken and widen, whereas the characteristic peaks of rhombohedral-In_2O_3 are enhanced with the overall decrease of the In_2O_3 crystallinity. As illustrated in Fig. 3a, the phase transition from cubic-In_2O_3 to rhombohedral-In_2O_3 was achieved by adjusting the In:Zn molar ratio. To be specific, rhombohedral-In_2O_3 possesses a larger electrical conductivity with a corresponding high EPSC magni-

tude. As shown in Fig. 3b, the transition from cubic-In_2O_3 to rhombohedral-In_2O_3 can be achieved by introducing Zn^{2+}. The specific reasons why excessive rhombohedral-In_2O_3 increases the energy consumption of NFNTs are as follows. Compared with cubic-In_2O_3, rhombohedral-In_2O_3 has a unique structure [39], which provides more channels for electron transport. Moreover, the electron mobility of rhombohedral-In_2O_3 is 2–5 times that of cubic-In_2O_3, resulting in a higher conductivity [40]. The main reason for the increase of carrier mobility is that the porosity of rhombohedral-In_2O_3 decreases slowly with the formation of nano/micro aggregates as well as the increased grain size. In addition, cubic-In_2O_3 and rhombohedral-In_2O_3 possess different band gaps, and this induces a new self-building electric field between the interfaces of cubic-In_2O_3 and rhombohedral-In_2O_3 nanocrystals [15], further promoting the interfacial charge transfer and enhancing the electrical conductivity of the device. Combining these two factors, the $In_{0.6}Zn_{0.4}O$ NFNT exhibits a higher EPSC magnitude compared with that of the $In_{0.7}Zn_{0.3}O$ NFNT.

Decreasing the transistor power consumption is paramount to improving the neuromorphic transistor performance. Based on the aforementioned discussion, we eventually determined the optimized In:Zn molar ratio to be 7:3, which is balanced by the combined factors of charge carrier concentration and crystal phase change. To further investigate the detailed structure of the $In_{0.7}Zn_{0.3}O$ NFAs, we also systematically carried out SEM, TEM and HRTEM measurements. Fig. 3c shows a typical SEM image of the $In_{0.7}Zn_{0.3}O$ NFAs obtained after UV illumination and calcination, in which the nanofibers exhibit uniform diameter distribution and smooth surface morphology. Fig. S4 demon-
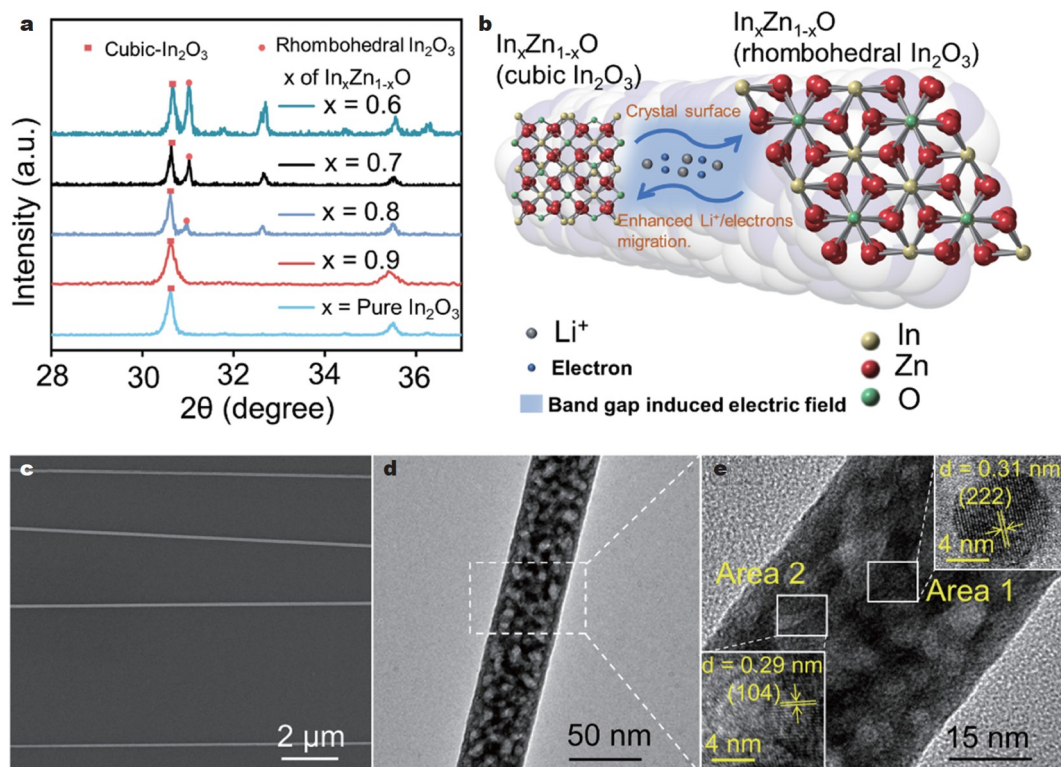

Figure 3 (a) XRD curves of pure In_2O_3 compared with $In_xZn_{1-x}O$ ($x = 0.6, 0.7, 0.8, 0.9$) nanofibers. (b) Schematic illustration of the enhanced electron transportation mechanisms of the cubic-In_2O_3 and rhombohedral-In_2O_3. (c) Typical SEM image of the $In_{0.7}Zn_{0.3}O$ NFAs. (d) TEM image of an $In_{0.7}Zn_{0.3}O$ nanofiber. (e) HRTEM image of the $In_{0.7}Zn_{0.3}O$ nanofiber. Inset: area 1 shows the lattice spacings of 3.1 Å corresponding to the (222) plane of rhombohedral-In_2O_3 and area 2 shows the lattice spacings of 2.9 Å corresponding to the (104) plane of cubic-In_2O_3.

strates that the diameter of $In_{0.7}Zn_{0.3}O$ nanofibers prepared by electrospinning falls in the range of 50–65 nm. The detailed NFA fabrication process can be found in the EXPERIMENTAL SECTION. The TEM image in Fig. 3d demonstrates the nanostructure of a single $In_{0.7}Zn_{0.3}O$ nanofiber. As depicted in Fig. 3e, area 1 and area 2 illustrate the lattice fringes with a d-spacing of 3.1 and 2.9 Å, which correspond to the (222) planes of cubic-In_2O_3 and the (104) planes of rhombohedral-In_2O_3, respectively. These results are in good agreement with the XRD analysis. Moreover, Fig. 3e shows perfect lattice matching between neighboring crystals in the rhombohedral-In_2O_3 and cubic-In_2O_3, resulting in enhanced interfacial charge transfer. All the atoms of In, Zn, and O are uniformly distributed along the nanofiber axially and radially, as demonstrated in the EDS mapping of Fig. S5.

Comparison of synaptic plasticity in devices with various In:Zn ratios

After elaborating the mechanism of optimal proportion formation, in this subsection we will compare the electrical perfor-

mance of $In_{0.6}Zn_{0.4}O$, $In_{0.7}Zn_{0.3}O$, $In_{0.8}Zn_{0.2}O$ and $In_{0.9}Zn_{0.1}O$ NFNTs. Fig. 4a demonstrates the transfer curves of NFNTs with $In_{0.6}Zn_{0.4}O$, $In_{0.7}Zn_{0.3}O$, $In_{0.8}Zn_{0.2}O$ and $In_{0.9}Zn_{0.1}O$ at a read voltage (V_{ds}) = 1 V, respectively. The NFNTs exhibit specific properties in the transfer curve for low-power neuromorphic devices, e.g., the S/D current I_{ds} near 0 V is low, which can determine the resting potential of EPSCs. As shown in Fig. S6, the leakage current is several orders of magnitude lower compared with the saturation current. Fig. 5a–d show typical EPSCs of $In_xZn_{1-x}O$ NFNTs, and the EPSCs are triggered by V_{gs} with an amplitude of 1 V and pulse width (t_p) of 50 ms, at a V_{ds} of 0.7 V. To be specific, when the pulse voltage is applied, the EPSC rises rapidly to a peak value. When the pulse voltage is removed, the EPSC gradually reduces to the resting value. This is because the lithium ions rapidly move to the interface between InZnO nanofibers and the electrolyte under the applied gate voltage, resulting in a sudden current increase. After removing the gate voltage, the ions gradually return to the electrolyte from the interface, thus restoring the current to the initial state. In comparison, the EPSC magnitude of $In_{0.7}Zn_{0.3}O$ NFNTs is the

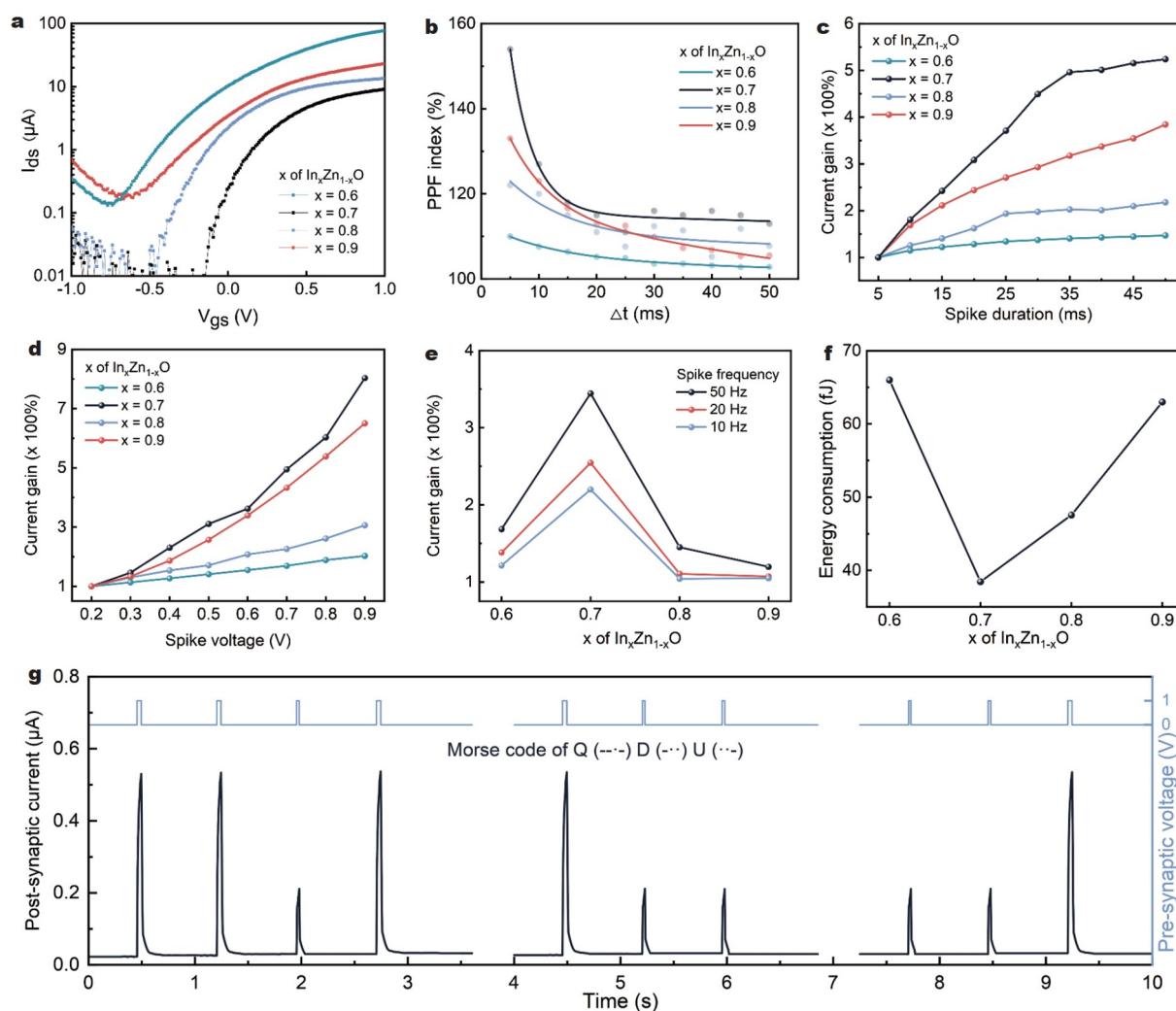**Figure 4** Emulated biological synaptic functions achieved by artificial synapses based on $In_xZn_{1-x}O$ (x = 0.6, 0.7, 0.8, 0.9) NFAs. (a) Transfer curves obtained with a read voltage V_{ds} of 1 V. (b) PPF index plotted as a function of Δt. The EPSCs were triggered by (c) pulse width from 5 to 50 ms, (d) pulse voltages ranging from 0.2 to 0.9 V and (e) frequencies at 10, 20 and 50 Hz. (f) Minimum energy consumption for single-synaptic events in $In_xZn_{1-x}O$ transistors. (g) 'QDU' Morse code displayed by $In_{0.7}Zn_{0.3}O$ NFNTs, at V_{gs} = 0.6 V and V_{ds} = 0.7 V. The output currents of <0.2 µA and >0.5 µA are defined as "dot (·)" and "dash (-)", respectively.
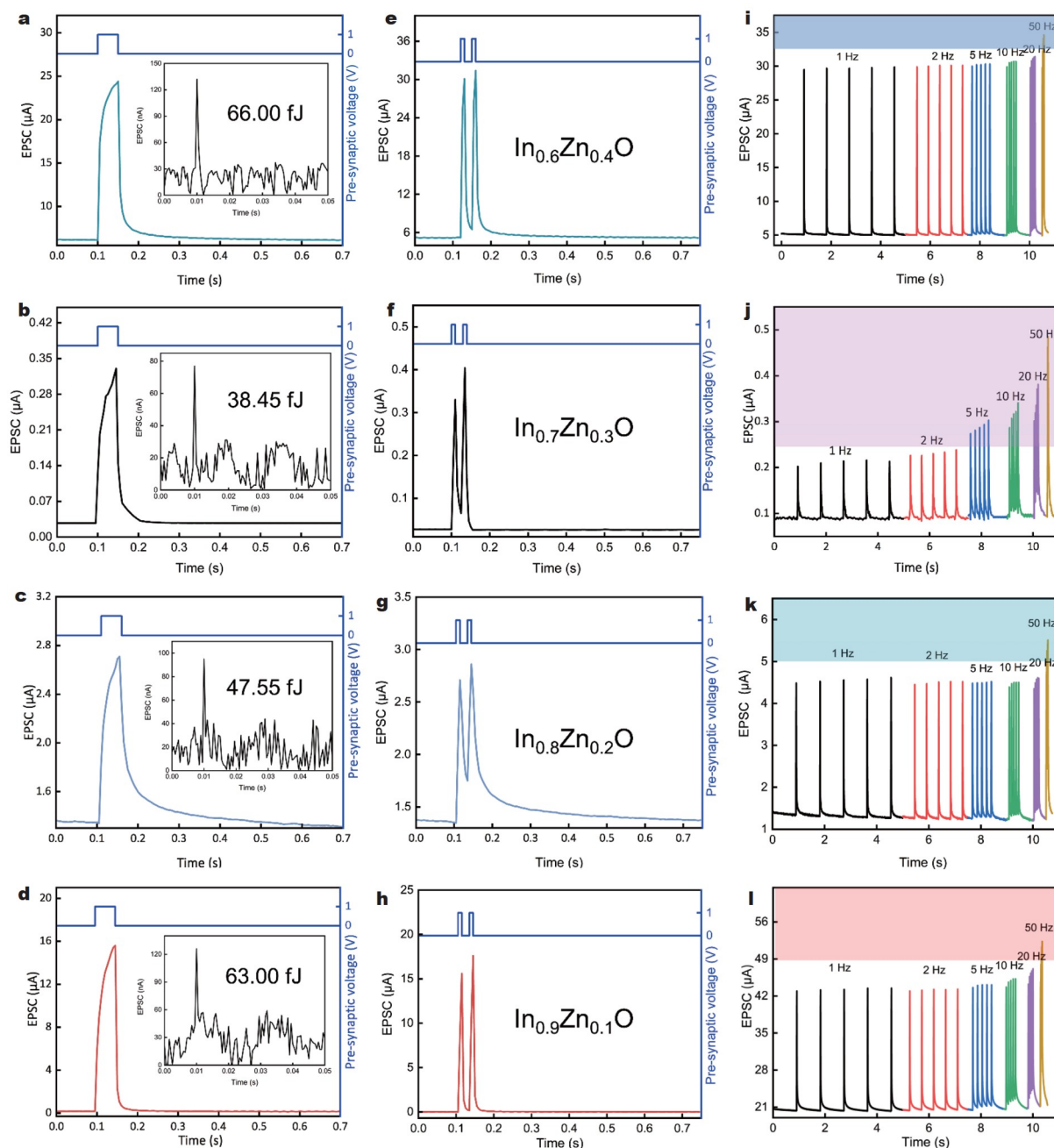
Figure 5 Emulated biological synaptic functions achieved by artificial synapses based on $In_xZn_{1-x}O$ NFNTs. (a–d) EPSCs obtained in applied V_{gs} with the amplitude of 1 V and t_p of 50 ms at V_{ds} of 0.7 V. Inset: energy consumption of a single synaptic event obtained in applied V_{gs} with the amplitude of 0.2 V and t_p of 0.05 ms at the small signal V_{ds} of 0.01 V. (e–h) PPF obtained in applied V_{gs} with the amplitude of 1 V, t_p of 20 ms and the time interval of 10 ms between the two signals at V_{ds} of 0.7 V. (i–l) Spike frequency-dependent plasticity obtained in an applied V_{gs} with the amplitude of 1 V and t_p of 10 ms at V_{ds} of 0.7 V.

lowest among the various In:Zn ratio combinations, due to positive impacts of a higher carrier concentration and more rhombohedral phase. This will be elaborated in a later section. To prove the environmental stability of the device, we measured the transfer curve and EPSC of $In_{0.7}Zn_{0.3}O$ NFNT after 10, 20 and 120 days, respectively. Fig. S7 shows that the transfer curves and EPSCs basically coincide, proving that the devices exhibit good stability.

The paired-pulse facilitation (PPF) is another factor to determine short-term synaptic plasticity, in which the synaptic response can be enhanced by two consecutive signals with a

short interval. Fig. 5e–h present typical PPF curves of $In_xZn_{1-x}O$ NFNTs, which are triggered by V_{gs} with an amplitude of 1 V, t_p of 20 ms and the time interval (Δt) of 10 ms between the two signals at V_{ds} of 0.7 V. The EPSC initiated by the first stimulus declines before the second stimulus arrives because the ions gradually diffuse back to their equilibrium status. When the second pulse stimulus arrives, if the ions induced by the first stimulus have not returned to the equilibrium status, the remaining ions can be superimposed onto the second current peak. This can increase the number of mobile ions triggered by the second stimulus. The curve of PPF index as a function of Δt

described in Fig. 4b can be fitted with the following exponential function [41]:

$$PPF = 1 + C_1\exp\left(-\frac{\Delta t}{\tau_1}\right) + C_2\exp\left(-\frac{\Delta t}{\tau_2}\right), \quad (1)$$

where C_1 and C_2 are the initial amplitudes of the first and second EPSC, τ_1 and τ_2 are the corresponding characteristic relaxation times, and Δt is the time interval between two pulses. It can be observed in Fig. 4b that the PPF indices of the four devices decrease with increased time interval. Table S2 presents that the In$_{0.7}$Zn$_{0.3}$O NFNT exhibits the maximum value of the PPF index, which is elucidated in the section of "Selection of low-power In$_x$Zn$_{1-x}$O (x = 0.6, 0.7, 0.8, 0.9) NFAs".

To further evaluate the EPSC response, the relationship between the EPSC with different pulse widths and pulse voltages was examined in Fig. 4c, d, respectively. Fig. 4c provides the dependence of EPSC on the V_{gs} width when the V_{gs} amplitude is set at 0.6 V while maintaining a V_{ds} = 0.7 V. As the pulse width increases, it takes a longer time for the cations in the electrolyte to move to the electrolyte/InZnO interface, with subsequent more charge carriers for a gradual increase in EPSC. The limited ion migration is responsible for the slow increase or even saturation of the EPSC response. Furthermore, to investigate the dependence of EPSC on the pulse voltage, the t_p was set to 50 ms while maintaining a V_{ds} of 0.7 V. As shown in Fig. 4d, when the V_{gs} amplitude increases from 0.2 to 0.9 V with a step of 0.1 V, the EPSC amplitude increases with increased pulse voltage.

Due to the fact that the PPF is highly correlated with the time interval between successive pulses, the EPSC response has obvious selectivity for successive signals of different frequencies. The probability of vesicles releasing neurotransmitters depends on the frequency of stimulation in synapses. Vesicles with low release probability respond to higher frequency signal stimuli, which correspond to the high-pass filtering function of the synapse. In general, the short-term synaptic enhancement behavior, such as PPF, contributes to achievement of high-pass filtering. Correspondingly, the EPSC responses of In$_x$Zn$_{1-x}$O (x = 0.6, 0.7, 0.8, 0.9) NFNTs with different signal frequencies were investigated while a V_{gs} with an amplitude of 1 V and a t_p of 10 ms at a V_{ds} of 0.7 V were held constant. The result is displayed in Fig. 5i–l. It can be observed that the In$_{0.7}$Zn$_{0.3}$O NFNT demonstrates significantly different EPSC responses to signal stimulations of different frequencies. The amplitude of EPSC increases from 0.22 µA at 1 Hz to 0.49 µA at 50 Hz, showing selectivity for high-frequency signals. The amplitude of 0.25 µA is set as the low frequency threshold current, whereas 0.40 µA is

treated as the high frequency threshold current. It can be observed from Fig. 4e that the current gain of In$_{0.7}$Zn$_{0.3}$O NFNT is more obvious than the gain in the other three devices.

Figs 4 and 5 compare the synaptic plasticity of the In$_x$Zn$_{1-x}$O NFNTs. At different pulse widths, pulse voltages and frequencies, the devices exhibit spike duration-dependent plasticity, spike voltage-dependent plasticity and spike frequency-dependent plasticity. Similar to living organisms, the learning and memory effects of the synaptic devices are closely related to the learning time, number of times and frequency of learning. Morse code is an on-off signal code that uses different sequences to transmit information. We carried out an experiment to generate Morse code using synaptic properties to illustrate the practical application of synaptic devices in information communication processing, as shown in Fig. 4g, which simulates the Morse code of the letter "Q", "D", and "U". The pulse widths of "dash -" and "dot ·" are 35 and 20 ms, respectively.

Based on the above comparison, the In$_{0.7}$Zn$_{0.3}$O NFNT exhibits the lowest EPSC peak compared with the other three devices at the same biasing condition, which suggests the low energy consumption of In$_{0.7}$Zn$_{0.3}$O NFNT. As shown in the inset of Fig. 5a–d, the EPSC peaks obtained from the In$_x$Zn$_{1-x}$O NFNTs under the same biasing conditions are 132, 76.9, 95.1 and 126 nA, respectively. The energy consumptions of In$_{0.6}$Zn$_{0.4}$O, In$_{0.7}$Zn$_{0.3}$O, In$_{0.8}$Zn$_{0.2}$O and In$_{0.9}$Zn$_{0.1}$O NFNTs are 66.00, 38.45, 47.55 and 63.00 fJ, respectively, as demonstrated in Fig. 4f. The power consumption has been calculated using the following formula [42]:

$$P = I_{peak} \times V \times t, \quad (2)$$

where I_{Peak} is the peak current of the EPSC, V is the read voltage, and t is the applied pulse width. Table 1 lists the power consumption of the InZnO NFNTs, which clearly demonstrates the low power consumption of the In$_{0.7}$Zn$_{0.3}$O NFNT.

Application: Identifying handwritten digits

To demonstrate the application of our devices for neuromorphic computing in handwriting recognition, Fig. S8a exemplifies a machine learning simulation of a neural network based on measured potentiation/depression *via* CrossSim. To fully illustrate the high linearity and the low noise capabilities of the In$_x$Zn$_{1-x}$O NFNTs, a three-layer artificial neural network (ANN) was simulated to perform supervised learning on a small image version (8 × 8 pixels) and the large image version (28 × 28 pixels) of the modified handwritten digits from the Modified National Institute of Standards and Technology (MNIST), as

Table 1 Energy consumption of single InZnO synaptic event

InZnO	Synthesis method	Electrolyte	Consumption (fJ)	Reference
Thin film	RF magnetron sputtering	Nanogranular SiO$_2$	1.80×10^5	[43]
Thin film	RF magnetron sputtering	Sodium alginate	1.35×10^4	[44]
Thin film	RF magnetron sputtering	Methylcellulose	1.60×10^7	[45]
Thin film	RF magnetron sputtering	Li$_{1.3}$Al$_{0.3}$Ti$_{0.7}$(PO$_4$)$_3$/PVP	2.28×10^3	[46]
Thin film	Thermal evaporation	C$_3$N$_4$/PVP	3.20×10^5	[7]
NFs (x = 0.6)	Electrospinning	LiClO$_4$/PEO	66.00	This work
NFs (x = 0.7)	Electrospinning	LiClO$_4$/PEO	38.45	This work
NFs (x = 0.8)	Electrospinning	LiClO$_4$/PEO	47.55	This work
NFs (x = 0.9)	Electrospinning	LiClO$_4$/PEO	63.00	This work

shown in Fig. S8b [47].

For neuromorphic calculations, the recognition accuracy depends on the linearity and symmetry of the weight updates, as well as the number of effective conductance states [48]. The 100 positive gate voltage of 0.2 V and the 100 negative gate voltage of −0.2 V were applied on the In$_x$Zn$_{1-x}$O NFNTs. All the pulse widths were maintained at 15 ms. Fig. 6a shows the potentiation and depression characteristics of the four devices after they were normalized to 100 pulses. To further study the weight update rule for handwritten digits and digital image recognition in the ANN simulation, the potentiation/depression curve was fitted using the weight update equation, and a nonlinearity of the

potentiation/depression curve was obtained.

$$G_{n+1} = G_n + \Delta G_P = G_n + \alpha_P \exp\left(-\beta_P \frac{G_n - G_{min}}{G_{max} - G_{min}}\right), \quad (3)$$

$$G_{n+1} = G_n + \Delta G_D = G_n - \alpha_D \exp\left(-\beta_D \frac{G_{max} - G_n}{G_{max} - G_{min}}\right), \quad (4)$$

where G_{n+1} and G_n represent the conductance values obtained after applying the $(n + 1)$th and nth pulses, α and β represent the conductance step change and nonlinearity, G_{max} and G_{min} represent the maximum and minimum conductance values, respectively. The data with respect to the nonlinearity of the four devices are summarized in Table S2. Equations (3) and (4)
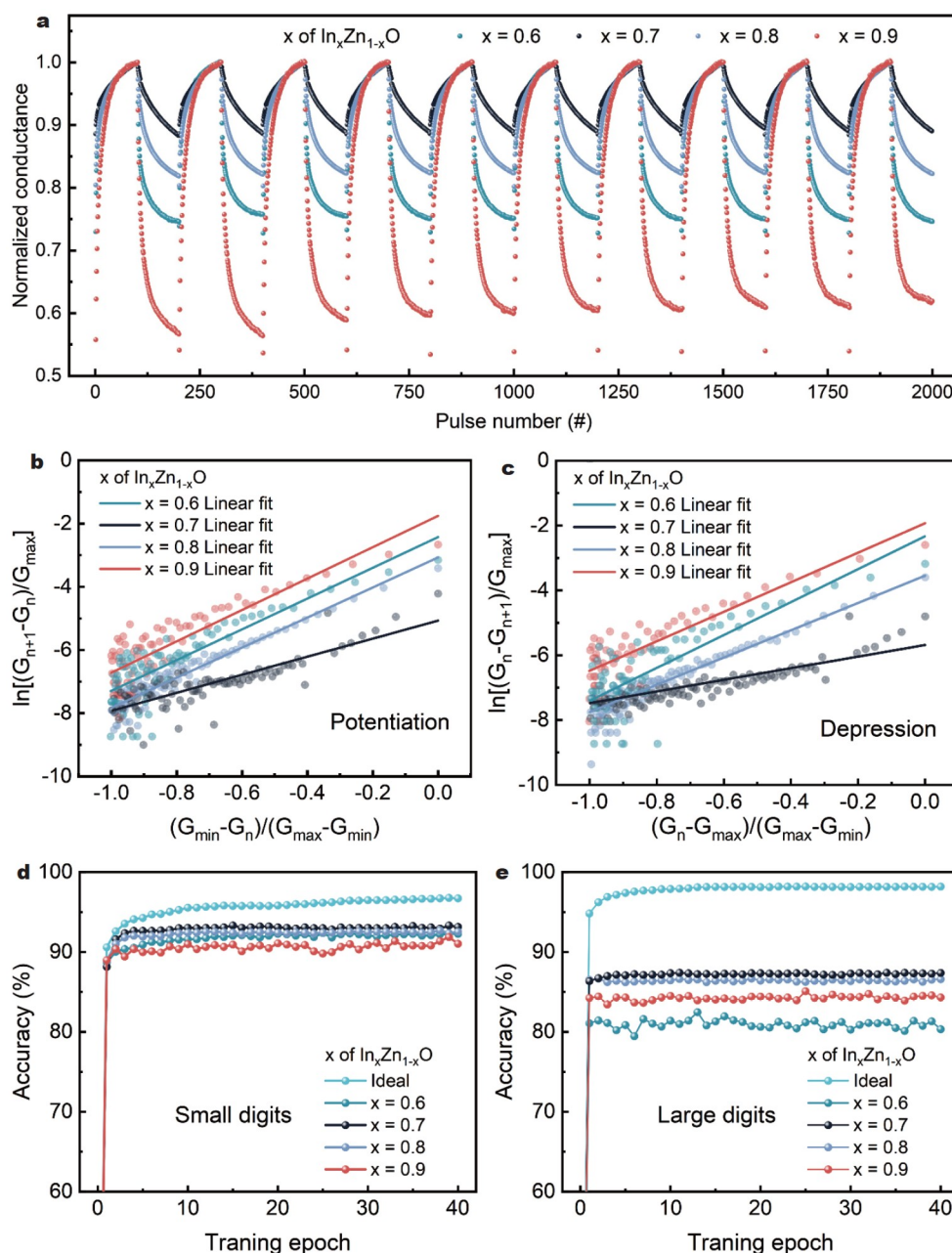

Figure 6 (a) Conductance updates of the In$_x$Zn$_{1-x}$O (x = 0.6, 0.7, 0.8, 0.9) NFNTs over 10 cycles, measured by consecutive gate pulses of 100 potentiation and 100 depression under the same condition (V_{gs} = 0.2 V for potentiation, V_{gs} = −0.2 V for depression). Processed experimental (b) potentiation and (c) depression data as well as the corresponding fitting curves. Recognition accuracy evolution with training epochs for 28 × 28 pixels handwritten digit images for (d) small handwritten digits and (e) large handwritten digits, respectively.

indicate that a smaller β correlates with a more linear weight update. The nonlinearity of the potentiation/depression curve fitting of the $In_xZn_{1-x}O$ NFNTs is shown in Fig. 6b, c, in which the $In_{0.7}Zn_{0.3}O$ NFNT exhibits better linear characteristics compared with the other three devices. Fig. 6d, e describe the variation of the recognition accuracy of handwritten digits with the training hours for the small-image and large-image versions, respectively. Therefore, compared with the other three devices, the handwriting recognition of $In_{0.7}Zn_{0.3}O$ NFNT exhibits a higher accuracy.

CONCLUSIONS

In this study, we have for the first time focused on systematically tuning the cation ratio of InZnO-based NFNTs, fabricated by low-cost electrospinning technique and a facile nanofiber transfer process. Among the cation ratios of $In_xZn_{1-x}O$ ($x = 0.6$, 0.7, 0.8, 0.9), we found that NFNTs based on $In_{0.7}Zn_{0.3}O$ exhibited the lowest EPSCs, and offered electrical benefits for low-power operation and synaptic function simulation. The reasons include two aspects that were revealed by the XPS and XRD measurements: (1) the content of oxygen vacancies can decrease with increased Zn content, leading to reduced free charge carrier concentration and subsequent low EPSC magnitude; (2) the rhombohedral hexahedral phase of In_2O_3 with better conductivity gradually dominates as the Zn content increases. The balancing point of these two impacts with subsequent excellent neuromorphic characteristics indicates that the rational tuning of MOS nanofiber composition opens the door for high-performance low-power NFNTs.

1   Pei J, Deng L, Song S, *et al.* Towards artificial general intelligence with hybrid Tianjic chip architecture. Nature, 2019, 572: 106–111

2   Ling H, Koutsouras DA, Kazemzadeh S, *et al.* Electrolyte-gated transistors for synaptic electronics, neuromorphic computing, and adaptable biointerfacing. Appl Phys Rev, 2020, 7: 011307

3   Liu X, Wang F, Su J, *et al.* Bio-inspired 3D artificial neuromorphic circuits. Adv Funct Mater, 2022, 32: 2113050

4   Cheng Y, Li H, Liu B, *et al.* Vertical 0D-perovskite/2D-MoS$_2$ van der Waals heterojunction phototransistor for emulating photoelectric-synergistically classical pavlovian conditioning and neural coding dynamics. Small, 2020, 16: 2005217

5   Seo S, Kim B, Kim D, *et al.* The gate injection-based field-effect synapse transistor with linear conductance update for online training. Nat Commun, 2022, 13: 6431

6   Han JK, Yun SY, Lee SW, *et al.* A review of artificial spiking neuron devices for neural processing and sensing. Adv Funct Mater, 2022, 32: 2204102

7   Li J, Yang YH, Chen Q, *et al.* Aqueous-solution-processed proton-conducting carbon nitride/polyvinylpyrrolidone composite electrolytes for low-power synaptic transistors with learning and memory functions. J Mater Chem C, 2020, 8: 4065–4072

8   Liu D, Shi Q, Dai S, *et al.* The design of 3D-interface architecture in an ultralow-power, electrospun single-fiber synaptic transistor for neuromorphic computing. Small, 2020, 16: 1907472

9   Zhang C, Wang S, Zhao X, *et al.* Sub-femtojoule-energy-consumption conformable synaptic transistors based on organic single-crystalline nanoribbons. Adv Funct Mater, 2021, 31: 2007894

10 Du C, Ren Y, Qu Z, *et al.* Synaptic transistors and neuromorphic systems based on carbon nano-materials. Nanoscale, 2021, 13: 7498–7522

11 Ercan E, Lin YC, Yang WC, *et al.* Self-assembled nanostructures of quantum dot/conjugated polymer hybrids for photonic synaptic tran-sistors with ultralow energy consumption and zero-gate bias. Adv Funct Mater, 2022, 32: 2107925

12 Hua Z, Yang B, Zhang J, *et al.* Monolayer molecular crystals for low-energy consumption optical synaptic transistors. Nano Res, 2022, 15: 7639–7645

13 Xie P, Huang Y, Wang W, *et al.* Ferroelectric P(VDF-TrFE) wrapped InGaAs nanowires for ultralow-power artificial synapses. Nano Energy, 2022, 91: 106654

14 Gao X, Zhang T. An overview: Facet-dependent metal oxide semiconductor gas sensors. Sens Actuat B-Chem, 2018, 277: 604–633

15 Song L, Dou K, Wang R, *et al.* Sr-doped cubic In_2O_3/rhombohedral In_2O_3 homojunction nanowires for highly sensitive and selective breath ethanol sensing: Experiment and DFT simulation studies. ACS Appl Mater Interfaces, 2020, 12: 1270–1279

16 Ouyang W, Teng F, He JH. Enhancing the photoelectric performance of photodetectors based on metal oxide semiconductors by charge-carrier engineering. Adv Funct Mater, 2019, 29: 1807672

17 He J, Xu P, Zhou R, *et al.* Combustion synthesized electrospun InZnO nanowires for ultraviolet photodetectors. Adv Elect Mater, 2022, 8: 2100997

18 Park JW, Kang BH, Kim HJ. A review of low-temperature solution-processed metal oxide thin-film transistors for flexible electronics. Adv Funct Mater, 2020, 30: 1904632

19 Wang Z, He Z, Lei C, *et al.* Phase transition enhanced thermoelectric performance for perovskites: The case of $AgTaO_3$. Curr Appl Phys, 2023, 48: 84–89

20 Zhu Y, Mao H, Zhu Y, *et al.* Photoelectric synapse based on InGaZnO nanofibers for high precision neuromorphic computing. IEEE Electron Device Lett, 2022, 43: 651–654

21 Chen B, Sun S, Fan S, *et al.* Low-cost fabricated MgSnO electrolyte-gated synaptic transistor with dual modulation of excitation and inhibition. Adv Elect Mater, 2022, 8: 2200864

22 Xin S, Chang Y, Zhou R, *et al.* Ultraviolet-driven metal oxide semiconductor synapses with improved long-term potentiation. J Mater Chem C, 2023, 11: 722–729

23 Yu JJ, Liang LY, Hu LX, *et al.* Optoelectronic neuromorphic thin-film transistors capable of selective attention and with ultra-low power dissipation. Nano Energy, 2019, 62: 772–780

24 Li L, Shao Y, Wang X, *et al.* Flexible femtojoule energy-consumption In-Ga-Zn-O synaptic transistors with extensively tunable memory time. IEEE Trans Electron Devices, 2020, 67: 105–112

25 Cho SI, Jeon JB, Kim JH, *et al.* Synaptic transistors with human brain-like fJ energy consumption *via* double oxide semiconductor engineering for neuromorphic electronics. J Mater Chem C, 2021, 9: 10243–10253

26 Gogurla N, Kim S. Self-powered and imperceptible electronic tattoos based on silk protein nanofiber and carbon nanotubes for human-machine interfaces. Adv Energy Mater, 2021, 11: 2100801

27 Chu PH, Kleinhenz N, Persson N, *et al.* Toward precision control of nanofiber orientation in conjugated polymer thin films: Impact on charge transport. Chem Mater, 2016, 28: 9099–9109

28 Zhu C, Wu J, Yan J, *et al.* Advanced fiber materials for wearable electronics. Adv Fiber Mater, 2023, 5: 12–35

29 Liu X, Miao J, Fan Q, *et al.* Recent progress on smart fiber and textile based wearable strain sensors: Materials, fabrications and applications. Adv Fiber Mater, 2022, 4: 361–389

30 Kim SJ, Jeong JS, Jang HW, *et al.* Dendritic network implementable organic neurofiber transistors with enhanced memory cyclic endurance for spatiotemporal iterative learning. Adv Mater, 2021, 33: 2100475

31 Chang Y, Cong H, Zhou R, *et al.* Enhanced artificial synaptic properties enabled by arrays of electrolyte-gated electrospun InZnO nanowires. ACS Appl Electron Mater, 2022, 4: 2570–2579

32 Zhu Y, Peng B, Zhu L, *et al.* IGZO nanofiber photoelectric neuro-morphic transistors with indium ratio tuned synaptic plasticity. Appl Phys Lett, 2022, 121: 133502

33 Cai X, Zhu P, Lu X, *et al.* Electrospinning of very long and highly aligned fibers. J Mater Sci, 2017, 52: 14004–14010

34 Greengard P. The neurobiology of slow synaptic transmission. Science, 2001, 294: 1024–1030

35 Ye JT, Inoue S, Kobayashi K, *et al.* Liquid-gated interface super-conductivity on an atomically flat film. Nat Mater, 2010, 9: 125–128

36 Yang Y, Hua H, Lv Z, *et al.* Reconstruction of electric double layer for long-life aqueous zinc metal batteries. Adv Funct Mater, 2023, 33: 2212446

37 Wang J, Wang L, Feng J, *et al.* Long-term *in vivo* monitoring of chemicals with fiber sensors. Adv Fiber Mater, 2021, 3: 47–58

38 Sorescu M, Diamandescu L, Tarabasanu-Mihaila D, *et al.* Nanocrystalline rhombohedral In_2O_3 synthesized by hydrothermal and post-annealing pathways. J Mater Sci, 2004, 39: 675–677

39 Liu D, Lei W, Qin S, *et al.* Large-scale synthesis of hexagonal corundum-type In_2O_3 by ball milling with enhanced lithium storage capabilities. J Mater Chem A, 2013, 1: 5274–5278

40 Oprea A, Gurlo A, Bârsan N, *et al.* Transport and gas sensing properties of In_2O_3 nanocrystalline thick films: A Hall effect based approach. Sens Actuat B-Chem, 2009, 139: 322–328

41 Zucker RS, Regehr WG. Short-term synaptic plasticity. Annu Rev Physiol, 2002, 64: 355–405

42 Dai S, Wang Y, Zhang J, *et al.* Wood-derived nanopaper dielectrics for organic synaptic transistors. ACS Appl Mater Interfaces, 2018, 10: 39983–39991

43 Zhou J, Wan C, Zhu L, *et al.* Synaptic behaviors mimicked in flexible oxide-based transistors on plastic substrates. IEEE Electron Device Lett, 2013, 34: 1433–1435

44 Wan C, Li B, Feng P, *et al.* Indium-zinc-oxide neuron thin film transistors laterally coupled by sodium alginate electrolytes. IEEE Trans Electron Devices, 2016, 63: 3958–3963

45 Srivastava S, Blower PJ, Aubdool AA, *et al.* Cardioprotective effects of $Cu^{(II)}$ATSM in human vascular smooth muscle cells and cardiomyocytes mediated by Nrf2 and DJ-1. Sci Rep, 2016, 6: 7

46 Li J, Yang YH, Fu WH, *et al.* Flexible transparent InZnO synapse transistor based on $Li_{1.3}Al_{0.3}Ti_{0.7}(PO_4)_3$/polyvinyl pyrrolidone nanocomposites electrolyte film for neuromorphic computing. Mater Today Phys, 2020, 15: 100264

47 Huang F, Fang F, Zheng Y, *et al.* Visible-light stimulated synaptic plasticity in amorphous indium-gallium-zinc oxide enabled by monocrystalline double perovskite for high-performance neuromorphic applications. Nano Res, 2023, 16: 1304–1312

48 Wan Q, Shi Y. Neuromorphic Devices for Brain-Inspired Computing: Artificial Intelligence, Perception and Robotics. Berlin: Wiley-VCH, 2022

Author contributions   Cong H and Chang Y performed the experiments; Zhou R and Zhang W designed the samples; Cong H and Sun G performed the data analysis; Xu P and Qin Y synthesized and characterized the samples; Ramakrishna S contributed to the discussion; Cong H and Chang Y wrote the paper with support from Wang F and Liu X. All authors contributed to the general discussion, and have given approval to the final version of the manuscript.

Conflict of interest   The authors declare that they have no conflict of interest.

Supplementary information   Supporting data are available in the online version of the paper.

Haofei Cong is currently a Master candidate at Qingdao University. Her research interest focuses on low-dimensional optoelectronic materials and devices.

Yu Chang is currently a research intern at Fujian Institute of Research on Structure of Matter, Chinese Academy of Sciences. He received his Master's degree from Qingdao University in 2022. His research interest focuses on electrical and optical synapses and neuromorphic devices.

Xuhai Liu received his PhD degree in functional materials & nanotechnology from the University of Southern Denmark in 2013, and later worked at Technische Universitat Dresden in Germany, Nanjing University of Science & Technology, and Nanjing University of Information Science and Technology. He is currently an associate professor at Qingdao University, with research interests focusing on low-dimensional material-based optoelectronics and bioelectronics.

Fengyun Wang received her PhD degree in materials physics & chemistry from the City University of Hong Kong in 2012, and later worked as a research fellow. In 2013, she joined Qingdao University as a professor. Her research program aims to utilize chemistry, physics, materials science, and various engineering disciplines to synthesize low-dimensional metal oxide semiconductors, perovskites, and MXenes, for bioelectronics, photonics, and energy storage devices.

用于低功率神经形态晶体管的金属氧化物半导体纳米纤维中阳离子比例的合理调整

丛浩菲[1†], 常宇[1†], 周睿夫[2], 张文鑫[1], 孙广欣[1], 徐沛龙[1], 秦元斌[3], Seeram Ramakrishna[4], 刘旭海[2*], 王凤云[1*]

摘要 宽带隙金属氧化物半导体(MOS)纳米纤维神经形态晶体管(NFNTs)可以潜在地用于构建低功耗的仿生人工电路. 但文献中对于NFNTs所采用MOS的阳离子配比并没有给出详细的原因. 在本研究中,我们首次系统地研究了用低成本静电纺丝技术结合纳米纤维转移工艺制备的氧化铟锌(InZnO)基NFNTs的阳离子比例. 基于双阳离子InZnO纳米纤维的电驱动NFNTs可以大大简化实验过程. 在$In_xZn_{1-x}O$的阳离子比(x = 0.6, 0.7, 0.8, 0.9)中, 我们发现基于$In_{0.7}Zn_{0.3}O$的NFNTs表现出最低的兴奋性突触后电流, 可以为低功耗操作和突触功能模拟提供电效益. MOS纳米纤维成分的合理调整可以为高性能低功耗NFNTs提供新的思路.